



Unraveling Liquefying Ablation and Evaporation Phenomena in High-Enthalpy Flow by means of High-Fidelity Numerical Methods: Improved Modeling and Sensitivity Analysis

David Henneaux¹, Achraf El Harfoch², Pierre Schrooyen³, Julien Klauner⁴, Bruno Barros Dias⁵, Bernd Helber⁶, Thierry Magin⁷, Louis Walpot⁸

Abstract

The destructive re-entry of space debris such as upper-stage launchers and non-operational satellites involves a wide range of coupled thermo-chemical and thermo-mechanical ablation processes. Within the Design for Demise (D4D) paradigm, ensuring that disintegration leads to an admissible on-ground casualty probability requires a reliable prediction capability for these complex phenomena. Among the materials of concern, glassy components—commonly used in high-precision optics and scientific instruments—pose a particular challenge, as their ablation behavior involves melting, shear removal, and evaporation, with the coexistence of gas, liquid, and solid phases. A critical aspect of this behavior is the evaporation process and the subsequent injection of vaporized species into the surrounding high-temperature reactive flow, both of which remain insufficiently understood and difficult to model with confidence.

In this work, we develop advanced models and numerical strategies to describe these processes in detail. The governing equations are formulated for each phase, and the interface balances that couple them are derived with particular emphasis on evaporation modeling. A staggered coupling strategy is implemented to carry out simulations of a VKI's Plasmatron experiment performed on a quartz sample, representative of glassy materials.

The numerical results demonstrate good to very good agreement with experimental measurements, despite the complexity and multi-physics nature of the problem. The simulations provide new insight into the interplay between evaporation and the injection of species into the surrounding flow, shedding light on mechanisms that strongly influence the ablation rate. These results constitute a first validation of the proposed physical models and numerical methodology, and they open the way for broader application under different conditions. Future work will include sensitivity analyses to identify key parameters, as well as the consideration of more complex evaporation mechanisms to refine predictive capabilities for D4D applications.

HiSST-2025-0083
High-fidelity simulation of evaporation and liquefying ablation
Copyrig

¹Hypersonic flows and phase-changing materials, Cenaero, Gosselies, Belgium, david.hen-neaux@cenaero.be

²Aero-Thermo-Mechanics, Université Libre de Bruxelles, ULB, Brussels, Belgium, achraf.el.harfoch@ulb.be

³Aeronautics & Aerospace, The von Karman Institute for Fluid Dynamics, Sint-Genesius-Rode, Belgium, pierre.schrooyen@vki.ac.be

⁴Institute of Mechanics, Materials and Civil Engineering, Université catholique de Louvain, UCLouvain, Louvain-La-Neuve, Belgium, julien.klauner@uclouvain.be

⁵Thermal Protection Materials Branch (TSM), National Aeronautics and Space Administration, NASA Ames, Mountain View, United States, bruno.dias@nasa.gov

⁶Aeronautics & Aerospace, The von Karman Institute for Fluid Dynamics, Sint-Genesius-Rode, Belgium, bernd.helber@vki.ac.be

⁷Aero-Thermo-Mechanics, Université Libre de Bruxelles, ULB, Brussels, Belgium, thierry.ma-gin@ulb.be

⁸ESTEC, European Space Agency, ESA, Noordwijk, The Netherlands, Louis.Walpot@esa.int

Keywords: Liquefying ablation, Evaporation, Numerical simulation, Experimental validation

1. Introduction

The destructive re-entry of upper stages launchers and nonoperational satellites involves complex physico-chemical interactions between the impacting high-enthalpy flow and the degrading material. Similarly to ablative thermal protection systems (TPS), those objects are subjected to thermo-chemical and thermo-mechanical ablation processes for which a deep understanding and a prediction capability are required in the design phase. Contrary to TPS that are designed to sustain a maximal accumulated heat load, re-entering launchers and satellites must follow the Design for Demise (D4D) paradigm according to which the disintegration of the space debris shall lead to an admissible on-ground casualty probability threshold. Rethinking the design principles of such complex pieces to meet this threshold while ensuring their nominal operation requires a profound understanding of the processes at play. This work aims to contribute to this objective through the development of advanced models and simulation techniques, supported by validation with experimental data. It has been carried out in the framework of the ESA GSTP activity "Validation of Space Debris Demise Tools Using Plasma Wind Tunnel Testing and Numerical Tools" (led by the von Karman Institute, VKI), concluded beginning of 2025. This work specifically focuses on the thermo-chemical ablation of a class of materials that are hardly demisable, hence critical for the D4D strategy, which are the glassy materials that are typically found in high-precision optics (lenses, mirrors) and scientific equipment on-board of satellites. Those materials exhibit a peculiar ablation behavior involving melting, shear ablation and evaporation processes and the presence of three phases (gas, liquid, solid). Its modeling necessitates the formulation of various complex and interdependent physical mechanisms. In particular, the evaporation process and the subsequent injection of vaporized species into the surrounding gas warrant special attention, as they remain poorly understood and their modeling is subject to significant uncertainty. We therefore propose to investigate these aspects in the present work, that builds upon studies such as [25, 8, 7].

The structure of the paper is as follows. We first detail the physico-chemical models, presenting the governing equations in both the gas and condensed phases, together with the interface balance conditions. The numerical methodology is then briefly outlined. This is followed by the presentation and discussion of numerical results obtained for a configuration replicating an experimental setup. Finally, conclusions and perspectives are provided.

2. Physico-chemical models

2.1. Gas phase - compressible multispecies reactive models

The gas phase is governed by the chemical non-equilibrium (CNE) compressible multispecies Navier-Stokes equations [24]:

$$\frac{\partial \rho_{i}}{\partial t} + \nabla \cdot (\rho_{i} \mathbf{u}) = -\nabla \cdot \mathbf{J}_{i} + \dot{\omega}_{i}, \qquad \forall i \in S_{g}$$

$$\frac{\partial \rho \mathbf{u}}{\partial t} + \nabla \cdot (\rho \mathbf{u} \otimes \mathbf{u}) = -\nabla P + \nabla \cdot \boldsymbol{\tau}, \qquad (1)$$

$$\frac{\partial \rho E}{\partial t} + \nabla \cdot (\rho H \mathbf{u}) = -\nabla \cdot \mathbf{q} + \nabla \cdot (\boldsymbol{\tau} \cdot \mathbf{u}) + \dot{\omega}_{T}.$$

where S_g is the set of gaseous species, ρ_i is the partial density of species i, J_i is the species diffusion flux, u is the velocity vector, $\dot{\omega}_i$ is the production rate of species i due to chemical reactions, $\dot{\omega}_T$ is the heat release due to chemical reactions, P is the thermodynamic pressure equal to the sum of the partial pressures by Dalton's law, τ is the viscous stress tensor, q is the heat flux, E is the total energy, and E is the total enthalpy. The transport and thermodynamic properties as well as chemical reaction rates are provided through the interfacing of the gas solver with the Mutation++ library [26]. Further explanations follow below.

Transport properties The species diffusion flux J_i of species i follows a multispecies Fick's law with Ramshaw projection [23]:

$$\mathbf{J}_{i} = -\rho D_{i,m} \frac{M_{i}}{M} \nabla x_{i} + \rho y_{i} \sum_{j \in S_{q}} D_{j,m} \frac{M_{j}}{M} \nabla x_{j}, \tag{2}$$

where x_i and y_i are the molar and mass fractions of species i, respectively, M_i is the molar mass, M is the mean molar mass of the mixture, and $D_{i,m} = \frac{1-y_i}{\sum_{j \neq i} \frac{x_j}{D_{ij}}}$ is the effective diffusion coefficient of

species i in the mixture, with D_{ij} the binary diffusion coefficient between species i and j. The viscous stress tensor is defined as:

$$\tau = \mu \left[\nabla \mathbf{u} + (\nabla \mathbf{u})^T - \frac{2}{3} (\nabla \cdot \mathbf{u}) \mathbf{I} \right], \tag{3}$$

where μ is the dynamic viscosity.

The heat flux q is expressed as:

$$\mathbf{q} = -\lambda \nabla T + \rho \sum_{i} h_{i} y_{i} \mathbf{V}_{i}, \tag{4}$$

with λ the thermal conductivity of the mixture, h_i the enthalpy of species i, and $V_i = \frac{J_i}{\rho y_i}$ the diffusion velocity of species i.

Because the vaporized species we consider, i.e. Si, SiO and SiO₂, are not included in the default transport database of Mutation++, we had to provide two parameters, namely dipole polarizability and the effective number of electrons for those species, whose values are given in Table 3. Those parameters are used by Mutation++ in the phenomenological Pirani potential [22] through correlations formula given by [16] in order to evaluate the collision integrals appearing in the computation of the transport properties.

Thermodynamic properties For a mixture of ideal gases, the thermodynamic properties are the sum of the quantities for pure species weighted by the composition of the mixture. Therefore, the gas mixture energy, resp. enthalpy, is a linear combination of the species energy, resp. enthalpy,

$$e(T) = \sum_{i \in S_g} y_i e_i(T), \quad h(T) = \sum_{i \in S_g} y_i h_i(T).$$

The enthalpy of a pure species can be separated in sensible and chemical enthalpies,

$$h_i(T) = \underbrace{\int_{T_0}^T c_{p_i} \, \mathrm{d}T}_{\text{sensible}} + \underbrace{h_{f,i}^0}_{chemical} \,, \tag{5}$$

where c_{p_i} is the heat capacity at constant pressure and $h_{f,i}^0$ is the formation enthalpy defined at a chosen temperature T_0 . Therefore, in the energy equation, an additional term should consider the formation enthalpy of the species produced:

$$\dot{\omega}_T = -\sum_{i \in S_a} \dot{\omega}_i \, h_{f,i}^0. \tag{6}$$

We use the NASA-9 database [20] through Mutation++ to obtain the properties of pure species as a function of temperature.

Chemical kinetics A reversible chemical reaction r in the set of all homogeneous reactions in the gas \mathcal{R}_q can be expressed as

$$\sum_{i \in S_g} \nu'_{ir} B_i \Longrightarrow \sum_{i \in S_g} \nu''_{ir} B_i, \quad \forall r \in \mathcal{R}_g,$$
(7)

where B_i is the chemical symbol for species $i \in S_g$, and ν'_{ir} and ν''_{ir} are the forward and backward stoichiometric coefficients for species i in reaction r. From the law of mass action, the chemical production rate is

$$\dot{\omega}_i = M_i \sum_{r \in \mathcal{R}_g} \nu_{ir} \mathcal{P}_r, \quad \forall i \in S_g,$$
(8)

where $\nu_{ir} = \nu_{ir}'' - \nu_{ir}'$ and the rate of progress of reaction r is given by

$$\mathcal{P}_r = k_r^f \prod_{i \in S_a} \left(\frac{\rho_i}{M_i}\right)^{\nu'_{ir}} - k_r^b \prod_{i \in S_a} \left(\frac{\rho_i}{M_i}\right)^{\nu''_{ir}}, \quad \forall r \in \mathcal{R}_g,$$

$$(9)$$

which represents the direction of the reaction, i.e, going towards the destruction of the reactants (\mathcal{P}_r > 0) or products (\mathcal{P}_r < 0). The forward rate k_r^f follows an Arrhenius-type empirical law given by

$$k_r^f(T) = A T^{\beta} \exp\left(-\frac{\theta}{T}\right), \quad \forall r \in \mathcal{R}_g.$$
 (10)

The backward reaction rate satisfies the equilibrium relation

$$k_r^b(T) = \frac{k_r^f(T)}{K_{\text{eq.}r}(T)} \tag{11} \label{eq:kr}$$

with the equilibrium constant of the reaction $K_{eq,r}$. The chemical reaction rates are directly provided to the gas solver through the Mutation++ interfacing. The chemical reactions involving the vaporized species that are considered in this work are listed in Table 4.

2.2. Condensed phase - incompressible phase-transformation model

The condensed phase is modeled using the classical enthalpy—porosity formulation [6]. This set of equations is similar to the incompressible Navier—Stokes equations, with additional terms introduced to account for the solid—liquid phase change and the dynamics of the mushy zone:

$$\nabla \cdot \mathbf{u} = 0,$$

$$\rho \frac{\partial \mathbf{u}}{\partial t} + \rho \mathbf{u} \cdot \nabla \mathbf{u} = -\nabla P + \nabla \cdot \boldsymbol{\tau} + \mathsf{S}(\mathbf{u}),$$

$$\rho \frac{\partial H}{\partial t} + \rho \mathbf{u} \cdot \nabla H = \nabla \cdot (\kappa \nabla T),$$
(12)

where κ is the thermal conductivity. The viscous stress tensor for this incompressible flow is expressed as:

$$\tau = \mu \left(\nabla \mathbf{u} + \nabla \mathbf{u}^T \right). \tag{13}$$

The total enthalpy H is given by:

$$H = \int_{T_{cof}}^{T} c_p \, dT + f_l \Delta h_{\mathsf{m}},\tag{14}$$

where c_p is the specific heat capacity at constant pressure, f_l is the liquid mass fraction, Δh_m is the latent heat of fusion. To allow differentiation, the liquid fraction is defined as a smooth function of temperature near the melting point:

$$f_l = \frac{1}{2} \left[\tanh \left(\frac{T - T_m}{T_{\text{liq}} - T_{\text{sol}}} \right) + 1 \right], \tag{15}$$

where T_{liq} and T_{sol} are the characteristic temperatures of the fully liquid and fully solid states, respectively and T_m the average between the two. Finally, the momentum source term S(u) is expressed as a momentum sink term that penalizes flow in solid regions:

$$S(u) = -C \frac{(1 - f_l)^2}{f_l^3 + \epsilon} u$$
 (16)

where $C\sim 10^8$ is a penalization constant (Carman–Kozeny type) and $\epsilon\sim 10^{-3}$ avoids division by zero. The second term mimics the resistance to flow in solid or partially solid regions, treating them as a porous medium with vanishing permeability as $f_l\to 0$.

Thermophysical properties The thermodynamic and transport properties of the condensed phase, here SiO_2 , are implemented as polynomial functions of the temperature in Mutation++ whose coefficient are found by curve-fitting with empirical data, mostly coming from [21]. As examples, the curves of enthalpy and dynamic viscosity of SiO_2 are plotted in Fig. 4.

2.3. Interface balances

To couple the two sets of governing equations, Eq. 1 and Eq. 12, balance conditions at the interface are required. By considering a control volume around the interface, noted Γ , that includes both phases, one can express the generic so-called jumps conditions as follows [12]:

$$[[\varphi(\mathbf{u} - \mathbf{u}_{\Gamma})]] \cdot \mathbf{n}_{\Gamma} = [[\mathcal{F}]] \cdot \mathbf{n}_{\Gamma} + \mathcal{P}^{s}, \tag{17}$$

where φ is an intensive physical quantity, \mathbf{u}_{Γ} is the interface velocity (distinct from the fluid velocity if mass transfer occurs), \mathbf{n}_{Γ} is the interface normal vector, \mathcal{F} is the flux of the quantity coming from the phase bulk, and \mathcal{P}^s is the interface production/destruction term. Note that we neglect here the interfacial inertia as well as the line flux along the interface (responsible for instance for surface tension effects). The jump operator across the interface at a position $\mathbf{x} \in \Gamma$ for some quantity η defined in the bulk of each phase is given by

$$[[\eta]] = (\eta_c|_{\Gamma} - \eta_g|_{\Gamma}), \quad \text{with } \eta_k|_{\Gamma} = \lim_{\epsilon \to 0, \epsilon > 0} \eta(\mathbf{x} \pm \epsilon \mathbf{n}_{\Gamma}). \tag{18}$$

In the remaining of this section, the quantities identified as \bullet_g refer to the gas phase while the ones written as \bullet_c belong to the condensed phase. In this work, we do not solve the two sets of governing equations strongly coupled through those jumps conditions. We rely instead on a weak coupling in which each solver takes the quantities coming from the other as constant. The jumps thus become boundary conditions to be applied to each solver.

Gas interface boundary conditions By considering the mass species balance, momentum and total energy from the gas perspective, the boundary conditions we impose in the gas solver on the phase interface read as:

$$\begin{split} \mathbf{J}_{i,g} \cdot \mathbf{n}_{\Gamma} &= \rho_{i,g} \mathbf{u}_{g} \cdot \mathbf{n}_{\Gamma} - \dot{\omega}_{i,g,\Gamma}, \quad \forall i \in S_{g}, \\ \boldsymbol{\tau}_{g} \cdot \mathbf{n}_{\Gamma} &= \boldsymbol{\tau}_{c} \cdot \mathbf{n}_{\Gamma} + \dot{m}_{\Gamma} \left(\mathbf{u}_{g} - \mathbf{u}_{c} \right) + (p_{g} - p_{c}) \mathbf{I} \cdot \mathbf{n}_{\Gamma}, \\ T_{g} &= T_{l}, \\ \mathbf{u}_{g} &= \dot{m}_{\Gamma} / \rho_{g} \mathbf{n}_{\Gamma}, \end{split} \tag{19}$$

where I is the identity matrix and $\dot{\omega}_{i,g,\Gamma}$ is the production/destruction rate of species i at the interface, that can be split as evaporation/condensation reaction and catalytic reaction:

$$\dot{\omega}_{i,g,\Gamma}=\dot{\omega}_{i,g,\Gamma}^{\mathrm{evap}}+\dot{\omega}_{i,g,\Gamma}^{\mathrm{cata}}.$$
 (20)

The net mass flux across the interface is obtained by summing the production/destruction rates $\dot{\omega}_{i,g,\Gamma}$ of each species, i.e.

$$\dot{m}_{\Gamma} = \sum_{i \in S_g} \dot{\omega}_{i,g,\Gamma}^{\text{evap}} + \underbrace{\sum_{i \in S_g} \dot{\omega}_{i,g,\Gamma}^{\text{cata}}}_{=0}. \tag{21}$$

Let us remark that we impose two Neumann-type boundary conditions on the mass diffusion and momentum diffusion fluxes and two Dirichlet-type boundary conditions on the surface temperature and velocity. The condition on the temperature could have been replaced by a Neumann condition on the heat flux (both should be equivalent at convergence) but we obtained better convergence behavior with this choice.

Condensed phase interface boundary conditions Similarly, on the condensed phase side, we impose the following Neumann boundary conditions:

$$\begin{split} & \boldsymbol{\tau}_c \cdot \mathbf{n}_{\Gamma} = \boldsymbol{\tau}_g \cdot \mathbf{n}_{\Gamma} + \dot{m}_{\Gamma} \left(\mathbf{u}_c - \mathbf{u}_g \right) + (p_c - p_g) \mathbf{I} \cdot \mathbf{n}_{\Gamma}, \\ & (\boldsymbol{\tau}_c \cdot \mathbf{u}_c - \mathbf{q}_c) \cdot \mathbf{n}_{\Gamma} = (\boldsymbol{\tau}_g \cdot \mathbf{u}_g - \mathbf{q}_g) \cdot \mathbf{n}_{\Gamma} - \dot{m}_{\Gamma} \Delta h_{\mathsf{vap}} - \epsilon \sigma (T_c^4 - T_{\infty}^4), \end{split} \tag{22}$$

where ϵ is the surface emissivity, σ the Stefan-Boltzmann constant and T_{∞} a reference temperature. Δh_{vap} is the latent heat of vaporization. Note that in principle, the difference of total enthalpies, H_g-H_c , should be used instead of the latent heat, by taking care of using enthalpies defined relative to the same reference state. However, the approximation we do here, that is very common in the literature, is justified by the fact that the latent heat dominates the enthalpy jump at the interface, even when the interface temperature differs from the saturation temperature. Furthermore, let us observe that the interface mass balance, which is not directly present in the boundary conditions we specify for the liquid, is used to prescribe the velocity of the moving interface as

$$\mathbf{u}_{\Gamma} = \mathbf{u}_{c} - \frac{\dot{m}_{\Gamma}}{\rho_{c}}.\tag{23}$$

Evaporation and catalytic reactions Finally, to close the set of interface balance conditions, one needs to specify a model for $\dot{\omega}_{i,g,\Gamma}^{\mathrm{evap}}$ and $\dot{\omega}_{i,g,\Gamma}^{\mathrm{cata}}$. For the catalytic reactions, we rely on the so-called ` γ ` model via Mutation++ [4]. It describes catalytic reactions as macroscopic, non-elementary processes of the form:

$$B + B \longrightarrow B_2$$
.

In order to determine the chemical production term for this kind of catalytic reactions, a probability for recombination γ is defined for each recombining species B as:

$$\gamma = F_{rec}/F_{imp},$$

where F_{imp} is the flux of species B impinging the surface and F_{rec} is the flux of species recombining at the surface. This probability is the input parameter for the model. The catalytic reactions considered in this work, with their recombination probabilities, are listed in Table 2.

For what concerns the mass flux due to evaporation/condensation phase change, we opt for a generalized Hertz-Knudsen model of the form

$$\dot{\omega}_{i,g,\Gamma}^{\text{evap}} = \sqrt{\frac{M_i}{2\pi RT_{\Gamma}}} \left(\alpha_i^{\text{evap}} P_i^{\text{vap}} - \alpha_i^{\text{cond}} P_i \right), \tag{24}$$

where α_i^{evap} and α_i^{cond} are adjustable coefficients that can model out-of-equilibrium effects in the Knudsen layer adjacent to the surface, P_i^{vap} is the equilibrium vapor pressure of species i and P_i is the partial pressure of that species in the gaseous mixture [5]. This kinetic-based expression, by considering the dynamics between evaporation and condensation fluxes of particles, allows modeling non-equilibrium effects and resistance to interfacial mass transfer, contrary to thermochemical equilibrium models. The last ingredient we need is an expression for the vapor pressure as a function of temperature. We consider the August form of the Antoine equation,

$$P_i^{\mathsf{vap}}(T) = \exp\left(A_i - \frac{B_i}{T}\right),\tag{25}$$

where the coefficients A_i and B_i are coefficients fitting a curve $P_i^{\text{vap}}(T)$. This curve is here obtained for the single evaporation reaction $SiO_2(c) \Longrightarrow SiO_2(g)$ by minimizing the total Gibbs free energy of the combined gas—condensed system at fixed temperatures and pressures [8]. The evaporation parameters used for the simulation are listed in Table 2.

3. Numerical methods

The simulation performed in this work has been carried out with the multiphysics Argo platform developed by Cenaero [14], and interfaced with the open-source Mutation++ library. Argo offers high-order spatial discretization of the governing equations by means of a Discontinuous Galerkin (DG) scheme. Implicit time discretization is employed to deal with the stiff phenomena considered here. A first-order and explicit weak staggered coupling strategy is adopted to exchange information between the gas and the condensed phase solvers. The workflow is as follows. First, the gas solver is converged to a steady-state solution on a conformal mesh by performing time-marching. The gas quantities appearing

in Eq. 22 are saved and are interpolated by the condensed phase solver on the interface position. This solver runs an unsteady simulation and relies on the eXtended DG method to consider moving interface problem in an unfitted way, i.e. by keeping the mesh fixed and by tracking the interface with a level-set function [13]. Once the coupling time is reached, the condensed phase solver stops and transfers its quantities appearing in Eq. 19 to the gas solver. A conformal mesh is automatically regenerated based on the updated position of the interface by using the open-source mesher Gmsh [11]. The gas solver then starts again and the process continues. This strategy is illustrated in Fig. 1.

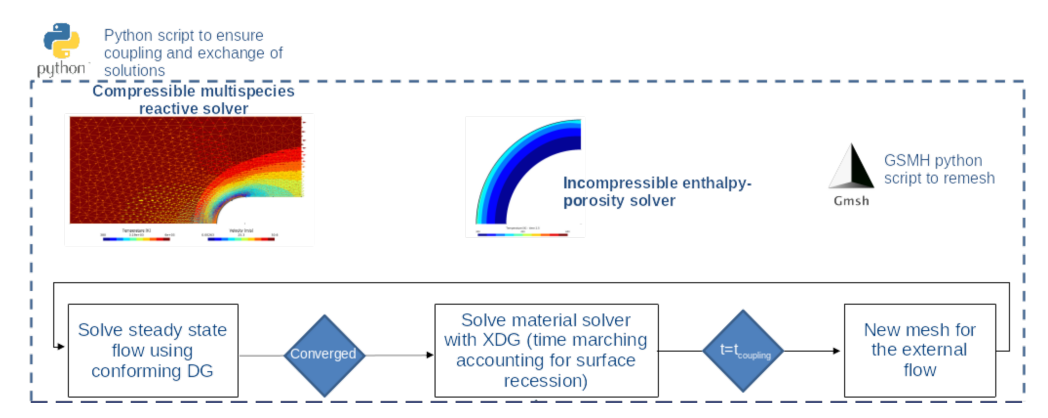


Fig 1. Workflow of the staggered solver adopting a weak coupling strategy between the gas and the material domains

4. Validation of numerical simulations against experimental data

4.1. Set-up

Experimental conditions and flight extrapolation The experimental test we propose to numerically replicate is the one conducted in the VKI's Inductively Coupled Plasma (ICP) Plasmatron facility on a hemispherical Quartz sample in subsonic conditions [10, 9]. The conditions characterizing this test are listed in Table 1 and are such that evaporation is expected to be the driving ablation mechanism (which has been confirmed experimentally). Note that while a complete duplication of re-entry flight conditions is not feasible around a scaled model in a ground facility, a local duplication can be achieved around the stagnation-point region following the Local Heat Transfer Simulation (LHTS) methodology [2]. This approach has been applied here to set the facility operating conditions.

$\dot{m}_{\sf gas}$	P_{el}	p_c	z	R	Test gas
g/s	kW	mbar	mm	mm	
16	292	100	385	25	Air

Table 1. Plasmatron test conditions. $\dot{m}_{\rm gas}$ the supplied mass flow rate of gas, $P_{\rm el}$ the electric power to the coil, p_c the chamber pressure, z the distance between the torch exit and the sample stagnation point, R the radius of the frontal hemisphere.

Simulation set-up The computational domain with the associated boundary conditions is presented in Fig. 2. As explained earlier, we rely on a loosely-coupled simulation framework in which the gas and the material domains exchange boundary conditions at some pre-defined frequencies, that are the following ones for the present case:

Exchange frequencies: $\{0, 0.25, 0.5, 1.5, 3.0, 5.0, 10.0, 20.0, 30.0, \dots, 190.0\}$ s.

We consider 2-D axisymmetric formulation. The gas domain inflow coincides with the exit of the Plasmatron torch. Our software Argo having not magneto-hydrodynamics models implemented yet,

we performed in a preliminary step a simulation with an in-house VKI's code solving the ICP equations in Local Thermodynamic Equilibrium (LTE) in the plasma torch [18]. We then extracted the flow profiles at the exit and injected those at the inflow of our simulation domain. Those inlet profiles are plotted in Fig. 3.

The list of the Quartz properties used for the simulation is provided in Table 2 while the transport properties and chemical kinetics parameters in the gas phase associated to the vaporized species are given in Table 3 and Table 4, respectively. Note that the thermodynamic properties of the mixture is obtained from the NASA9 database [20] implemented in Mutation++, that includes the vaporized species we consider. Finally, we consider the direct evaporation reaction,

$$SiO_2(I) \longrightarrow SiO_2$$

as the only evaporation mechanism. Although the inclusion of dissociative mechanisms is entirely feasible, our initial investigation focused on a single mechanism, as we found that adding dissociation significantly hampered the convergence of the gas solver. Let us note that from thermodynamic considerations, the principal evaporation mechanism for SiO_2 should be

$$SiO_2(I) \longrightarrow SiO + \frac{1}{2}O_2$$

but the direct mechanism has also been observed to be significant under certain circumstances [1].

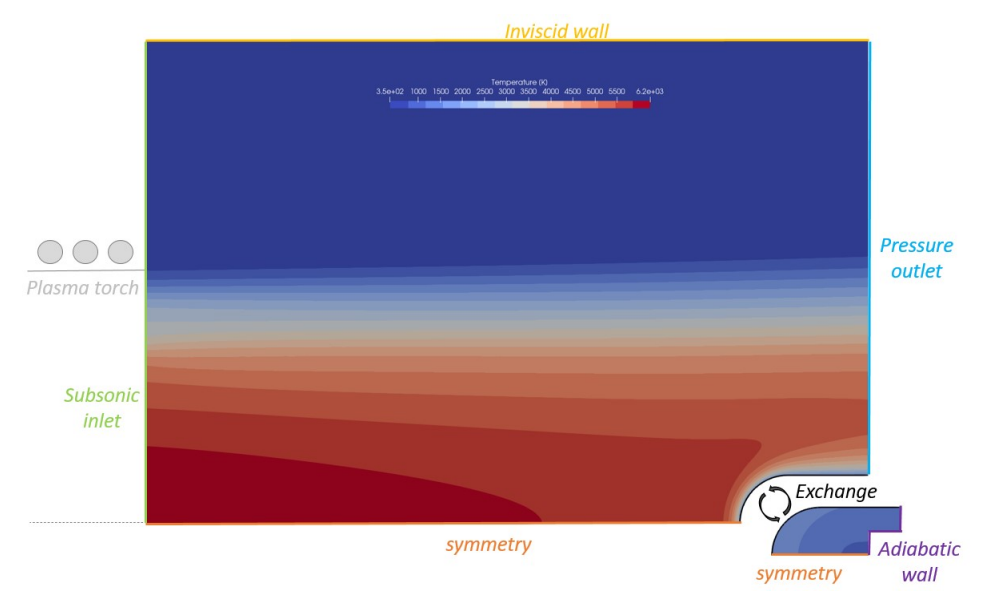


Fig 2. Numerical domain and boundary conditions used for the replication of the Plasmatron test case.

4.2. Simulation results

We simulate the experimental test case with the conditions and parameters described above. In Fig. 5, the comparison between the numerical predictions and the experimental measurements is done based on the stagnation point temperature and surface recession. For the surface temperature, the agreement is very good in the beginning of the transient phase and at steady-state with a temperature reaching a plateau value very close to the experimental one. For the rest of the transient temperature increase, the discrepancies that can be observed are likely due to the fact that we consider constant emissivity and catalytic recombination coefficients. This should be investigated in future studies. Concerning the stagnation point recession, an overall good matching is also obtained. However, the numerical curve deviates from the experimental linear trend starting from ~ 150 s. While further validation is required, we hypothesize that two principal sources could account for this deviation. The first one

	Input parameters	Notation	Value	Reference
	Dynamic viscosity	μ_{liq}	depends on T, see Fig. 4b	[27]
	Thermal conductivity	k	depends on T	[28]
	Enthalpy	h	depends on T, see Fig. 4a	[19]
_	Liquidus	T_{liq}	2100 K	[19]
eriż	Solidus	T_{sol}	1996 K	[19]
Material	Density	$ ho_{liq}$	$2200~{ m kg}{ m m}^{-3}$	Sample manufacturer
_	Molar mass	M_m	$60.08 \; {\rm g mol}^{-1}$	Periodic table
	Emissivity	ϵ	0.4	Measured in the experi-
				ments
	Latent heat of vaporiza- tion	$\Delta h_{\sf vap}$	$1.28~\mathrm{MJ}\mathrm{K}^{-1}$	
	Vapor pressure coeffs	A_{SiO2} , B_{SiO2}	29.8902 , 64645.8814 K	Multiphase equilibrium
	Evaporation coeff.	$lpha_{ extsf{SiO2}}^{ ext{evap}}$	1.0	
GSI	Condensation coeff.	$lpha_{ extsf{SiO2}}^{ extsf{cond}}$	1.0	
Ğ	Catalytic recombination	γ_{O}	0.03	[3]
	$0+0 \rightarrow 0_2$			
	Catalytic recombination	γ_{N}	0.03	[3]
	$N + N \longrightarrow N_2$			

Table 2. List of Quartz thermophysical properties used for the simulation

Species	α	N_{ee}	Ref
	${ m \AA}^3$		
Si	6.00003	3.3182145207364	[17]
SiO	4.43867	8.5277377164517	[17]
SiO ₂	4.47009	13.068565355797	[17]

Table 3. Dipole polarizability α and the number of effective electrons N_{ee} for the Pirani potential used to compute gas transport properties.

Reaction	Α	β	θ	Ref
	m,s,mol		K	
Si + NO ⇒ SiO + N	3.2×10^{13}	0.0	1775.0	[15]
$Si + O_2 \Longrightarrow SiO + O$	2.1×10^{15}	-0.53	16.83	[15]
SiO + M ← Si + O + M	4.0×10^{14}	0.0	95600.0	[15]
$SiO_2 + M \Longrightarrow SiO + O + M$	4.0×10^{14}	0.0	95600.0	[15]

Table 4. Arrhenius parameters for the gas-phase chemical reactions involving vaporized species. M represents any species in the mixture involved in heavy particle impact dissociation reaction.

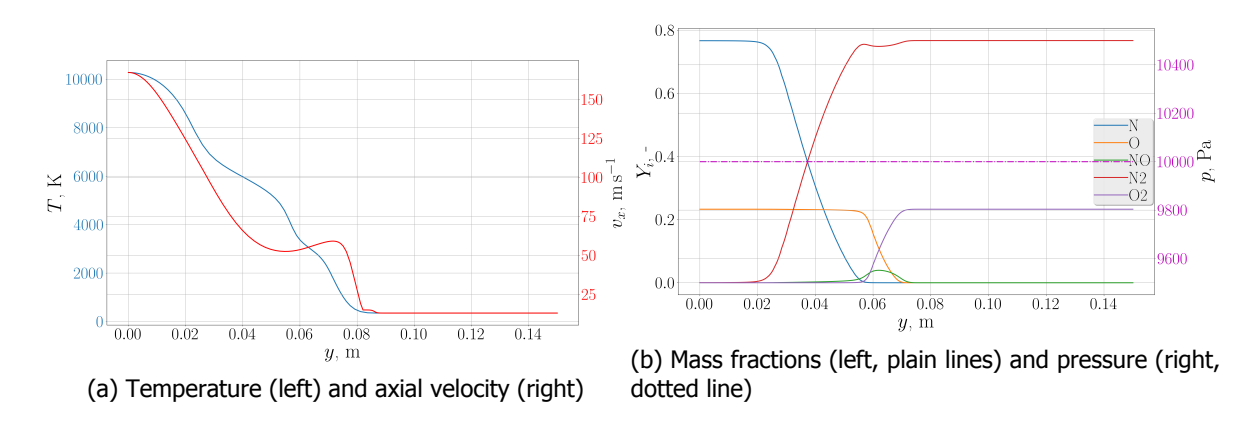


Fig 3. Profiles of quantities specified at the inlet of the gas computational domain, obtained from VKI's ICP computations.

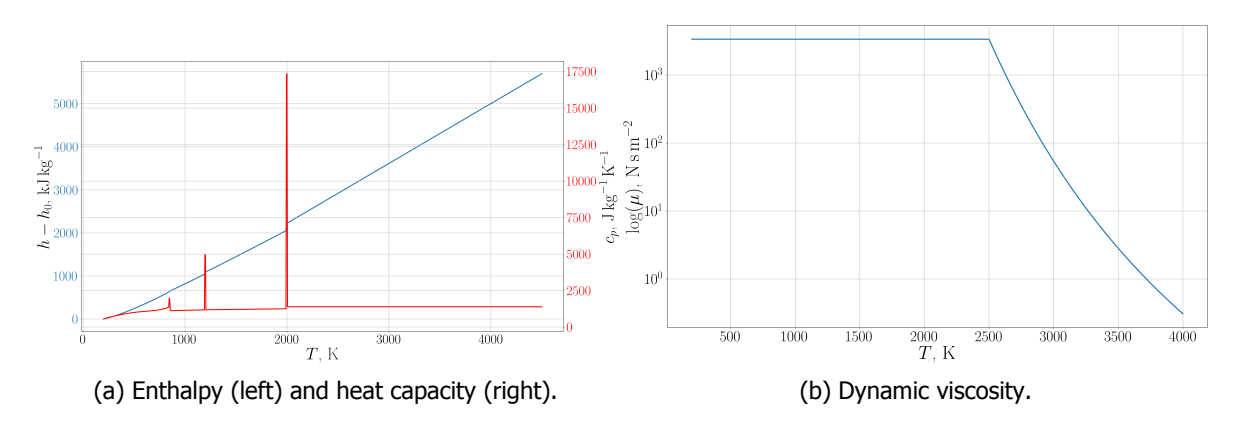


Fig 4. Properties of Quartz over a temperature range given by the correlations implemented in Mutation++.

would be the inaccuracies in the material properties employed, in particular the viscosity. Since the viscosity is the main driving parameter in the entrainment of the glassy material by the gas forces (more than the glass transition temperature itself), a deviation from its real value would affect the dynamics of the molten layer. The second potential reason would be the use of a simplified evaporation mechanism considering only the direct evaporation reaction $SiO_2(I) \longrightarrow SiO_2$ and not the dissociative ones. Beyond its impact on the net interface mass flux, the choice of evaporation mechanism also dictates which species are predominantly injected into the gas phase. This, in turn, can strongly affect the thermodynamics, transport properties, and chemical kinetics of the surrounding gas, thereby altering the local concentration of vaporized species at the material interface and ultimately influencing the condensation rate as described by the Hertz-Knudsen formula.

This is exemplified by the profiles of the vaporized species mole fractions along the sample surface and along the stagnation line in the gas in Fig. 6. The choice of the evaporation mechanism naturally leads to a much higher concentration of SiO₂, compared to the two other species that are created inside the gas through chemical reactions between SiO₂ and the air species. Because of the most intense heat flux around the stagnation region, the concentrations of SiO₂ and Si are the highest in that region, whilst the SiO remains almost constant along the sample. In the right figure, we can notice the diffusion of the vaporized species inside the gas phase, with SiO₂ being transported the further away from the interface and Si concentration reaching a peak slightly upstream of the stagnation point.

Experimental dynamic target shape tracking delivering in situ measurements of 2D ablation profiles allows to assess the numerical predictions of the whole sample shape in Fig. 7. Although the simulation

HiSST-2025-0083

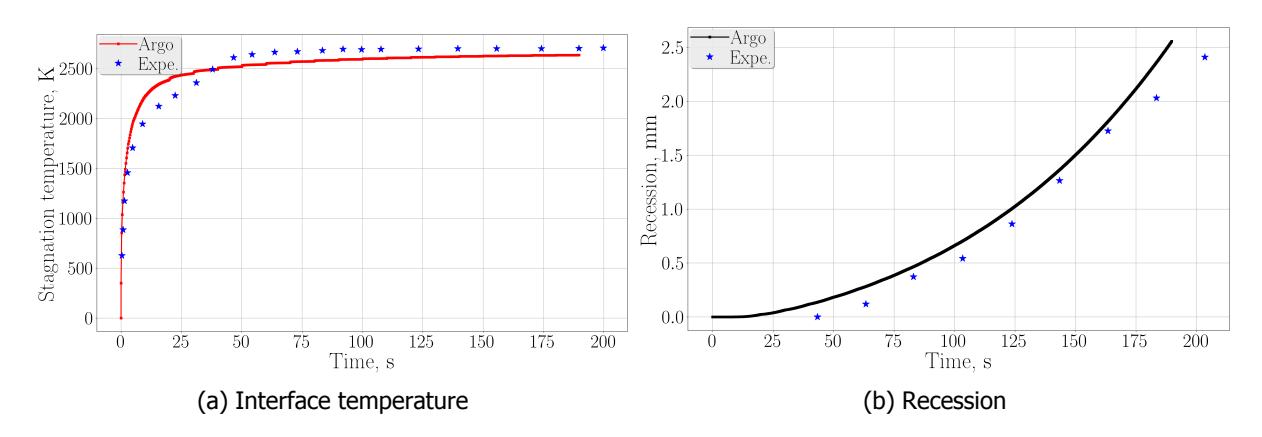


Fig 5. Numerical - experimental temporal comparison at the stagnation point.

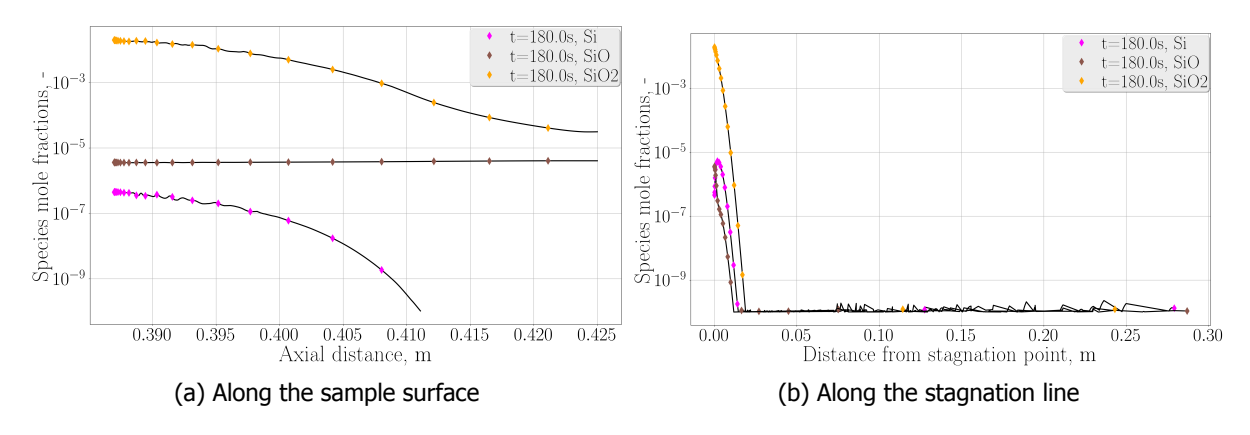


Fig 6. Numerical mole fractions of vaporized species at t=180s.

could not be extended over the entire experimental duration, it is worth noting that within the simulated time frame, the predicted recession around the stagnation point agrees well with the measurements. In addition, the slight bump observed in the experimental profile before x=25 mm is also captured by the simulation.

Finally, we close this results section with Fig. 8 that presents in the gas phase the SiO_2 partial pressure field and in the condensed phase, the velocity streamlines. Such a figure proves valuable in revealing specific characteristics of the gas-surface interactions and ablation process. We can observe the extent with which the vaporized SiO_2 is transported on one hand. On the other hand, we identify the region of the glassy material being entrained by the gas stresses, with the direction and magnitude of the velocity.

5. Conclusions and perspectives

In this work, we focused on the modeling and simulation of the detailed evaporation process involved in the liquefying ablation of materials immersed in high-temperature reactive flows. The governing equations were presented for each phase, together with the interface balances that couple them, with particular emphasis on highlighting the role of evaporation modeling.

To assess the proposed approach, we implemented a staggered coupling strategy and applied it to the simulation of a Plasmatron experiment on a quartz sample. The numerical results obtained show good to very good agreement with the experimental measurements, especially considering the complexity and variety of the phenomena involved. These simulations also provided valuable insight into the interplay between the evaporation process and the injection of vaporized species into the surrounding gas.

Overall, these encouraging results constitute a first validation of both the physical models and the

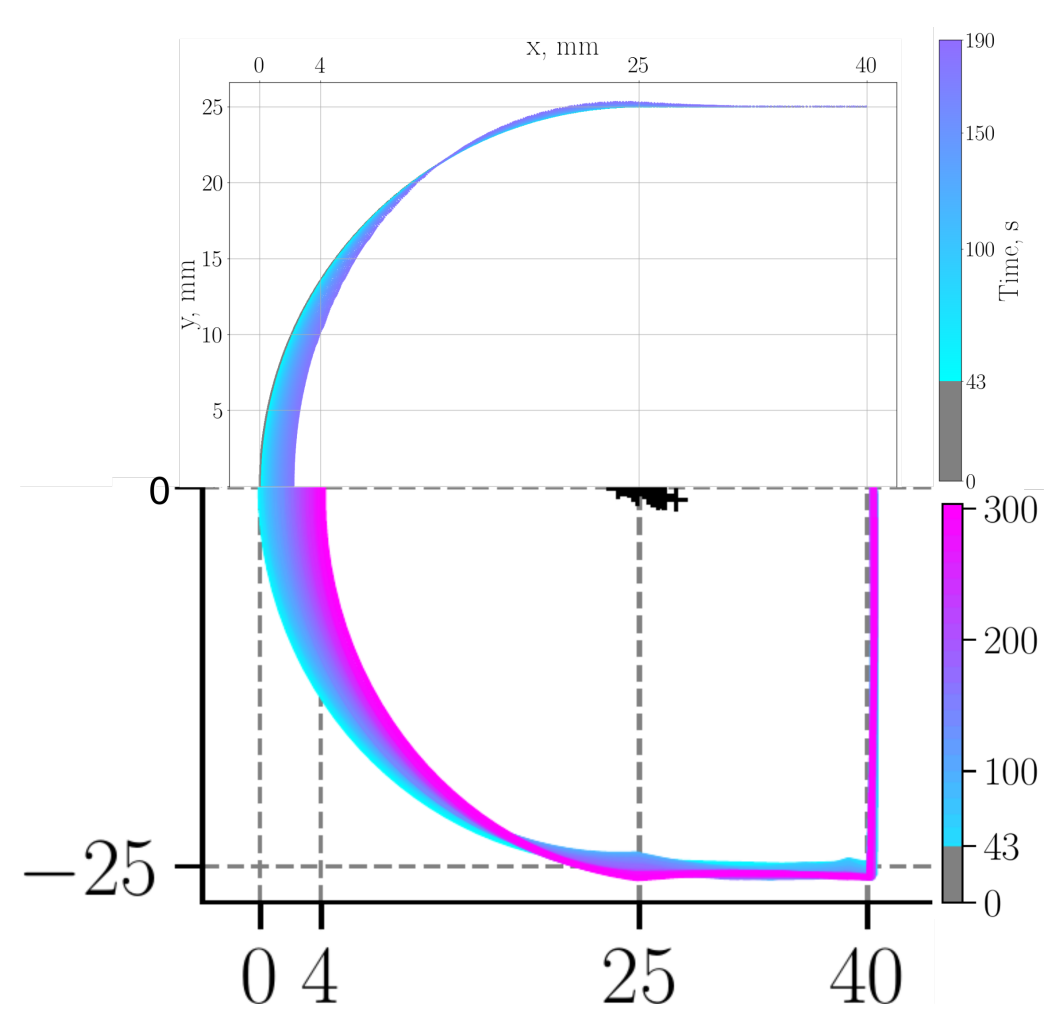


Fig 7. Temporal evolution of the sample shape. Comparison between numerical (top) and experimental (bottom) results, based on the same colormap. Experimental data taken from [9].

numerical methodology developed. They provide a solid foundation for extending the approach to other operating conditions and for refining the models further.

As perspectives, it would be of particular interest to conduct a sensitivity analysis to identify the most influential parameters. In addition, the inclusion of more complex evaporation mechanisms should be considered in order to assess their impact on both the ablation rate and the characteristics of the incoming gas flow.

References

- [1] CM O'D Alexander. Exploration of quantitative kinetic models for the evaporation of silicate melts in vacuum and in hydrogen. Meteoritics & Planetary Science, 36(2):255-283, 2001.
- [2] PAOLO FRANCESCO Barbante and O Chazot. Flight extrapolation of plasma wind tunnel stagnation region flowfield. Journal of Thermophysics and Heat Transfer, 20(3):493-499, 2006.
- [3] L Bedra, M Rutigliano, M Balat-Pichelin, and M Cacciatore. Atomic oxygen recombination on quartz at high temperature: experiments and molecular dynamics simulation. Langmuir, 22(17):7208-7216, 2006.
- [4] G Bellas. Development of advanced gas-surface interaction models for chemically reacting flows for re-entry conditions. PhD thesis, Ph. D. thesis, VKI/Politecnico di Milano, 2018.

HiSST-2025-0083

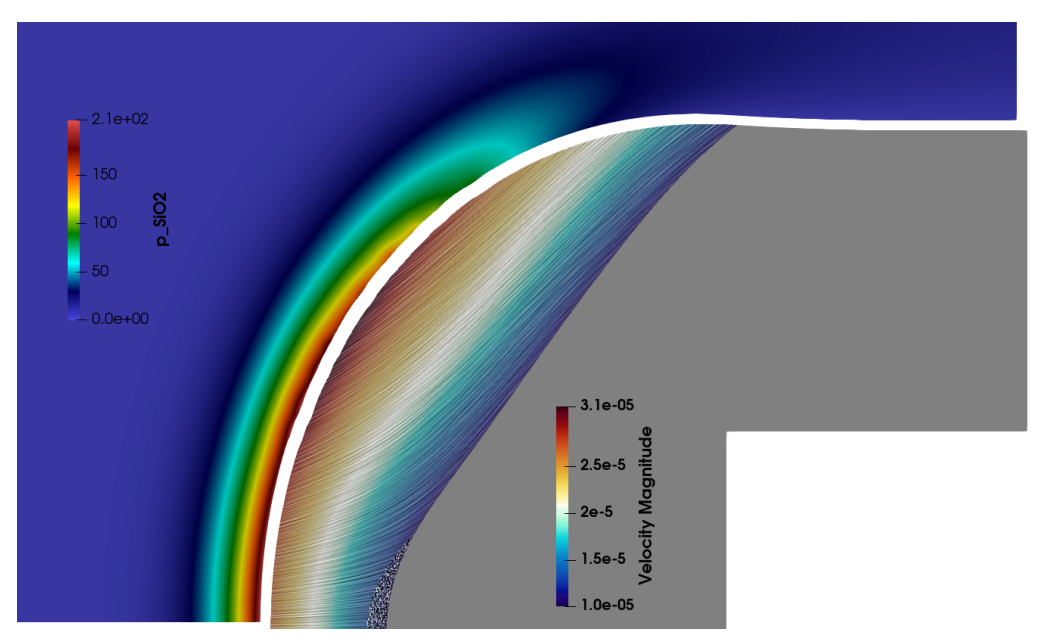


Fig 8. Partial pressure of vaporized SiO₂ in the gas phase and velocity streamlines colored by velocity magnitude in the material, with a lower threshold set to $1 \times 10^{-5} \text{m s}^{-1}$, at t = 190 s.

- [5] Maurice Bond and Henning Struchtrup. Mean evaporation and condensation coefficients based on energy dependent condensation probability. *Physical Review E—Statistical, Nonlinear, and Soft Matter Physics*, 70(6):061605, 2004.
- [6] Jean Sébastien Cagnone, Koen Hillewaert, and Nicolas Poletz. A discontinuous galerkin method for multiphysics welding simulations. *Key Engineering Materials*, 611:1319–1326, 2014.
- [7] Yih-Kanq Chen. Thermal ablation modeling for silicate materials. In *54th AIAA Aerospace Sciences Meeting*, page 1514, 2016.
- [8] Bruno Dias, Alessandro Turchi, Eric C Stern, and Thierry E Magin. A model for meteoroid ablation including melting and vaporization. *Icarus*, 345:113710, 2020.
- [9] Andrea Fagnani. Development of Measurement Techniques and Study of the Aerothermal Response of Space Debris Materials to Atmospheric Entry Plasmas. PhD thesis, Vrije Universiteit Brussel, 2023.
- [10] Andrea Fagnani, Bruno Dias, Pierre Schrooyen, Bernd Helber, Thierry E Magin, and Olivier Chazot. Investigation of quartz ablation in the vki plasmatron facility: Comparison between experimental and numerical results. In *AIAA Aviation 2021 Forum*, page 3137, 2021.
- [11] Christophe Geuzaine and Jean-François Remacle. Gmsh: A 3-d finite element mesh generator with built-in pre-and post-processing facilities. *International journal for numerical methods in engineering*, 79(11):1309–1331, 2009.
- [12] David Henneaux. A high-order discontinuous Galerkin tool for the simulation of multiphase problems: application to space debris ablation by melting. PhD thesis, Université Catholique de Louvain, 2024.
- [13] David Henneaux, Pierre Schrooyen, Philippe Chatelain, and Thierry Magin. High-order enforcement of jumps conditions between compressible viscous phases: an extended interior penalty discontinuous galerkin method for sharp interface simulation. Computer Methods in Applied Mechanics and Engineering, 415:116215, 2023.

- [14] Koen Hillewaert. Development of the discontinuous Galerkin method for high-resolution, large scale CFD and acoustics in industrial geometries. PhD thesis, Université Catholique de Louvain, 2013.
- [15] C. Johnston and E. Stern. Influence of coupled radiation and ablation on meteor entries. In *47th AIAA Thermophysics Conference*, pages AIAA 2017–4533, 2017.
- [16] A Laricchiuta, G Colonna, D Bruno, R Celiberto, Claudine Gorse, Fernando Pirani, and M Capitelli. Classical transport collision integrals for a lennard-jones like phenomenological model potential. *Chemical Physics Letters*, 445(4-6):133–139, 2007.
- [17] Antonio C Lasaga and Randall T Cygan. Electronic and ionic polarizabilities of silicate minerals. *American Mineralogist*, 67(3-4):328–334, 1982.
- [18] Thierry Magin. *A model for inductive plasma wind tunnels*. PhD thesis, Université libre de Bruxelles, 2004.
- [19] B. J. McBride, S. Gordon, and M. A Reno. Thermodynamic Data for Fifty Reference Elements. NASA TP-3287-REV1, Glenn Research Center, Cleveland, Ohio, February 2001.
- [20] Bonnie J McBride. Computer program for calculation of complex chemical equilibrium compositions and applications, volume 2. NASA Lewis Research Center, 1996.
- [21] Kenneth C Mills. Recommended values of thermophysical properties for selected commercial alloys. Woodhead publishing, 2002.
- [22] Fernando Pirani, M Alberti, A Castro, M Moix Teixidor, and D Cappelletti. Atom–bond pairwise additive representation for intermolecular potential energy surfaces. *Chemical Physics Letters*, 394(1-3):37–44, 2004.
- [23] John D Ramshaw. Self-consistent effective binary diffusion in multicomponent gas mixtures. *Journal of Non-Equilibrium Thermodynamics*, 1990.
- [24] P. Schrooyen. *Numerical Simulation of Aerothermal Flows through Ablative Thermal Protection Systems*. PhD thesis, Université catholique de Louvain, 2015.
- [25] Pierre Schrooyen, Bruno Dias, Andrea Fagnani, Alessandro Turchi, Bernd Helber, Louis Walpot, and Thierry Magin. Ablation modeling of liquefying materials. In 2nd International Conference on Flight Vehicles, Aerothermodynamics and Re-entry Missions & Engineering (FAR), 2022.
- [26] James B Scoggins, Vincent Leroy, Georgios Bellas-Chatzigeorgis, Bruno Dias, and Thierry E Magin. Mutation++: Multicomponent thermodynamic and transport properties for ionized gases in c++. SoftwareX, 12:100575, 2020.
- [27] G. Urbain, Y. Bottinga, and P. Richet. Viscosity of liquid silica, silicates and alumino-silicates. *Geochimica et Cosmochimica Acta*, 46(6):1061–1072, 1982.
- [28] Kurt L. Wray and Thomas J. Connolly. Thermal conductivity of clear fused silica at high temperatures. *Journal of Applied Physics*, 30(11):1702–1705, 1959.